Top-hat cw laser induced thermal mirror: a complete model for material characterization

Astrath, N. G. C.; Astrath, F. B. G.; Shen, J.; Zhou, J.; Gu, C. E.; Malacarne, L. C.; Pedreira, P. R. B.; Bento, A. C.; Baesso, M. L.

Publisher's version / Version de l'éditeur:
https://doi.org/10.1007/s00340-008-3310-1
Applied Physics B, 94, March 3, pp. 473-481, 2009

Appl Phys B (2009) 94: 473–481
DOI 10.1007/s00340-008-3310-1

Applied Physics B
Lasers and Optics

Top-hat cw laser induced thermal mirror: a complete model for material characterization

N.G.C. Astrath · F.B.G. Astrath · J. Shen · J. Zhou · C.E. Gu · L.C. Malacarne · P.R.B. Pedreira · A.C. Bento · M.L. Baesso

Received: 1 August 2008 / Revised version: 30 October 2008 / Published online: 22 November 2008

Abstract A complete theoretical model is presented for the thermal mirror technique under top-hat laser excitation. Considering the attenuation of the top-hat excitation laser intensity along the thickness of a sample due to its optical absorption coefficient, we calculate the laser-induced temperature and surface deformation profiles. A simplified theoretical model for a high absorption sample is also developed. The center intensity of a probe beam reflected from the thermal mirror at a detector plane is derived. Numerical simulation shows that the thermal mirror under the top-hat laser excitation is as sensitive as that under Gaussian laser excitation. With top-hat laser excitation, the experimental results of thermo-physical properties of opaque samples are found to be well consistent with literature values, validating the theory.

PACS 78.20.Nv · 78.47.+p · 65.60.+a

1 Introduction

Photothermal (PT) science and techniques have achieved enormous accomplishments from material characterization to chemical analyses [1–8]. PT techniques are based on the photo-induced heat generation following optical energy absorption by a sample, and the heat can cause a number of different effects. One of the most ordinary observed effects is the surface displacement or deformation. This phenomenon is introduced when a focused excitation laser beam shines on a solid material, resulting in expansion and then a local surface displacement of the solid sample. Several PT techniques were reported to sense the displacement for the purpose of material characterization. In the interferometric scheme proposed by Kuo and Munidasa [9], called surface thermal lens (STL) technique, a modulated pump beam is focused on the sample surface to produce the surface deformation, and an unfocused probe beam is incident at the deformation region. The spot size of the reflected probe beam at the sample surface is much larger than that of the pump beam, producing an interference or diffraction pattern at the detection plane. This method was applied to study optical properties of thin films, semiconductor materials, and characterization of other solid materials [10, 11]. Recently, we [12–14] theoretically and experimentally demonstrated the applications of photothermally induced nanoscale surface displacement (STL effect) for low [12, 14] and high [13, 14] optical absorption materials. In these works, the surface displacement was induced by a focused TEM_{00} Gaussian excitation laser, and the local surface displacement acted as a concave or convex mirror, namely thermal mirror (TM), to a second TEM_{00} laser impinging on the surface deformation. The surface deformation was dependent on the optical and thermo-mechanical properties of the sample and could be probed by the second laser reflected from it [12–14].

Notwithstanding the successful application of the TM method to study solid materials, the high cost of a TEM_{00} Gaussian laser as an excitation light source and its inadequate wavelength lines restrict the potential applications

N.G.C. Astrath · F.B.G. Astrath · J. Shen (✉) · J. Zhou · C.E. Gu
National Research Council of Canada, Institute for Fuel Cell Innovation, 4250 Wesbrook Mall, Vancouver, British Columbia V6T 1W5, Canada
e-mail: jun.shen@nrc-cnrc.gc.ca

N.G.C. Astrath
e-mail: astrathngc@pq.cnpq.br

L.C. Malacarne · P.R.B. Pedreira · A.C. Bento · M.L. Baesso
Departamento de Física, Universidade Estadual de Maringá, Avenida Colombo 5790, 87020-900 Maringá, PR, Brazil

of the TM and a variety of PT techniques [6, 7]. To remove the restriction, Li and coauthors introduced the top-hat laser beam excitation into the pulsed [15, 16] and modulated [17] excitation STL technique. Moreover, we presented [18] a theoretical model and experimental validation for time-resolved mode-mismatched thermal lens spectroscopy induced by a cw laser with a top-hat profile. Recently [19], it has been also introduced into the TM technique. A low absorption theoretical model for transparent samples, which does not consider the attenuation of excitation light through the sample thickness due to the optical absorption of the sample, was successfully developed and experimentally validated with glass samples. Regarding the current status of the applications of top-hat excitation to photothermal techniques, one may find a brief review in [19].

In order to expand the application of the top-hat laser excitation to the TM technique, in this paper, we report a general theory for the TM technique under top-hat laser excitation using Beer's law to take into account the attenuation of the excitation laser intensity along the thickness of the sample. A three-dimensional temperature rise in the sample and a thermoelastic displacement on the sample surface are derived by solving the heat conduction and thermoelastic equations. Fresnel diffraction theory is employed to calculate the propagation of the probe beam reflected from the TM that introduces an additional phase shift to the electrical field of the probe beam, leading to a time-resolved expression of the probe beam intensity at a detector plane. Theoretical models of two extreme cases, i.e., very low and very high optical absorption, are also compared with the general model with Beer's law, showing that the general model is a complete model covering these extreme cases, while the theories of the extremes simplify the calculation. Very good agreement between theoretical and experimental results is attained. In addition, the top-hat laser-induced temperature and displacement profiles obtained in this work are theoretically compared to that obtained using the TEM_{00} Gaussian laser excitation [13], showing that the top-hat laser excitation is as sensitive as the Gaussian one. Moreover, by using the top-hat laser excitation, the measured thermal and mechanical properties of three opaque samples are found to be in very good agreement with literature values.

2 Theory

Figure 1 shows the scheme of a mode-mismatched TM experiment. A top-hat cw excitation laser shines on a sample, causing the thermoelastic displacement. A weak TEM_{00} Gaussian beam, collinear with the excitation laser, is reflected by the sample surface displacement and probes the TM effect. The radii of the excitation and probe beams on the sample surface are ω_{0e} and ω_{1P}, respectively. The probe beam propagates in the z-direction, and the sample is located at $z = 0$. In this configuration, it is assumed that the sample dimensions are large compared with the excitation beam radius to avoid edge effects, and the surface displacement of the sample is short compared with the sample thickness.

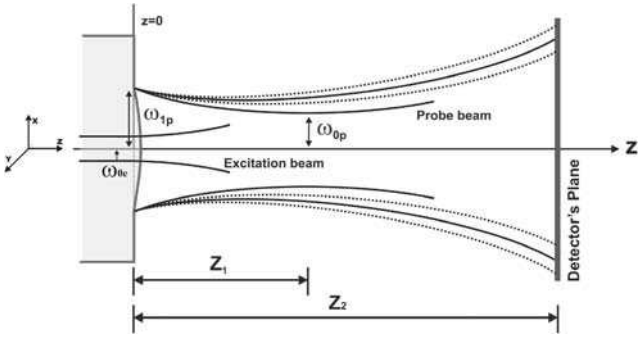

Fig. 1 A scheme of the geometric positions of the beams in a TM experiment. The distance between the sample and the plane of a TM detector is Z_2, and the distance between the sample and the probe beam waist of a radius ω_{0P} is Z_1

2.1 Temperature rise distribution

The distribution of the temperature rise, $T(r, z, t)$, in an isotropic sample is given by the solution of the heat conduction differential equation [19, 20]

$$c\rho\frac{\partial T(r,z,t)}{\partial t} - k\nabla^2 T(r,z,t) = Q(r,z), \tag{1}$$

with the initial condition $T(r, z, 0) = 0$ and the boundary conditions $T(\infty, z, t) = 0$ and $\partial T(r, z, t)/\partial z|_{z=0} = 0$. c, ρ and k are the specific heat, mass density, and thermal conductivity of the sample, respectively. The intensity of a top-hat excitation beam $I_{\mathrm{TH}}(r)$ and a TEM_{00} Gaussian one $I_{\mathrm{G}}(r)$ can be expressed as [13, 19]

$$\begin{aligned} I_{\mathrm{TH}}(r) &= \frac{P_e}{\pi\omega_{0e}^2}\mathbf{U}(\omega_{0e} - r), \\ I_{\mathrm{G}}(r) &= \tfrac{2P_e}{\pi\omega_{0e}^2}\exp\left(-2r^2/\omega_{0e}\right), \end{aligned} \tag{2}$$

in which P_e is the excitation laser power. The Unit-step function, $\mathbf{U}(x)$, is zero for a negative argument and one for a positive one. Figure 2 shows the intensity distributions for the top-hat and Gaussian profiles.

The top-hat heat source profile can be expressed as [19]

$$Q(r,z) = Q_0\mathbf{U}(\omega_{0e} - r)Q(z). \tag{3}$$

$Q_0 = P_e A_e \phi/\rho c\pi\omega_{0e}^2$; A_e is the optical absorption coefficient of the sample at the excitation laser wavelength, and $\phi = 1 - \eta\lambda_e/\langle\lambda_{\mathrm{em}}\rangle$. λ_e is the excitation beam wavelength, $\langle\lambda_{\mathrm{em}}\rangle$ the average wavelength of the fluorescence emission,

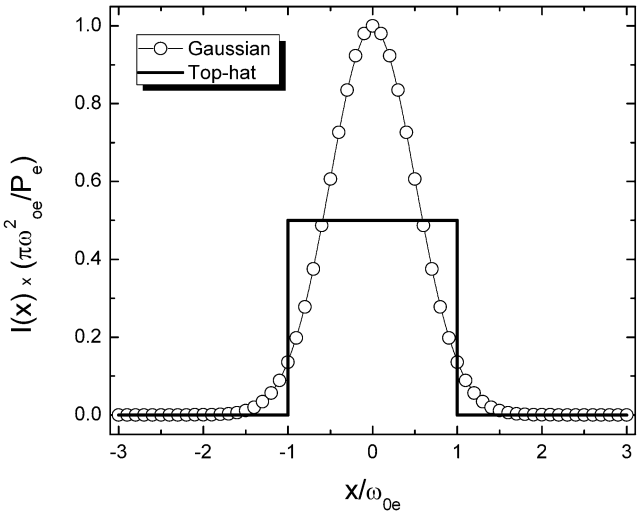

Fig. 2 Radial intensity distributions for the top-hat and Gaussian profiles with $y = 0$

and η is the fluorescence quantum efficiency, which competes for a share of absorbed excitation energy. Using Beer's Law, the z-dependence of the source term can be used to describe the optical absorption in the sample in the whole absorption coefficient range as $Q(z) = \exp(-A_e z)$. To distinguish this treatment from the low optical absorption model (LAM) [19] and the high absorption model (HAM) that will be presented later, we call it Beer's Law model (BLM).

Using the integral transform methods [12–19], the solution of heat conduction differential equation for the BLM is

$$T_{\mathrm{BLM}}(r,z,t) = \frac{T_0 A_e \omega_{0e}}{2} \int_0^\infty f_{\mathrm{BLM}}(a,z,t) J_0(r\alpha) J_1(\omega_{0e}\alpha)\, d\alpha \qquad (4)$$

with

$$f_{\mathrm{BLM}}(\alpha,z,t) = \int_0^t \left\{ \exp\left[\frac{(A_e-\alpha)(A_e+\alpha)\tau\omega_{0e}^2}{4t_c} - zA_e \right] \times \left[1 + \mathrm{Erf}\left(\frac{z - A_e\tau\omega_{0e}^2/2t_c}{\omega_{0e}\sqrt{\tau/t_c}} \right) + \exp(2zA_e)\,\mathrm{Erfc}\left(\frac{z + A_e\tau\omega_{0e}^2/2t_c}{\omega_{0e}\sqrt{\tau/t_c}} \right) \right] \right\} d\tau \qquad (5)$$

where $T_0 = P_e\phi/(4\pi k t_c)$. $\mathrm{Erfc}(x)$ is the complementary error function, and $J_n(x)$ is the n-order Bessel function of the first kind. $t_c = \omega_{0e}^2/4D$ is the characteristic thermal time constant, and $D = k/\rho c$ is the thermal diffusivity of the sample.

The Gaussian laser beam has been proven to be very sensitive [12–14] for TM measurements and applicable for a wide absorption coefficient range by using the BLM [12–14]. To show the applicability of the top-hat beam excitation and its sensitivity, in Fig. 3 we compare the temperature rise profiles on the surface of the sample ($z = 0$) produced by the top-hat beam with that caused by the Gaussian one for different exposure times. We used (4) for the top-hat beam excitation and (1) of [13] for the BLM Gaussian one, both normalized by T_0. $A_e = 1000\ \mathrm{m}^{-1}$ and $\omega_{0e} = 300\ \mu\mathrm{m}$ were used in the numerical calculations.

Figure 3 shows the normalized radial temperature rise profiles corresponding to the top-hat and Gaussian excitation laser beams, respectively. For a time less than a characteristic thermal time constant t_c the temperature profiles follow the excitation intensity profiles (as shown in Fig. 2), and the maximum temperature rise caused by the Gaussian excitation at the center of the beam is higher than that caused by the top-hat one. On the other hand, for $t = 50t_c$, the temperature profiles for both top-hat and Gaussian excitations are approximately the same. At the beam center, the temperature rise caused by the Gaussian excitation is slightly higher than that caused by the top-hat one.

Although the BLM describes the temperature behavior for a wide absorption coefficient range, the mathematical simplicity of the extreme cases is of interest for faster numerical calculations. One can find the TM low absorption model (LAM) in [19], and we develop the high absorption model (HAM) here. In the HAM, the z-dependence of the source term for a sample with extremely high absorption coefficient is $Q(z) = (2/A_e)\delta(z)$. By using the integral transform methods, the solution of heat conduction equation for the HAM at the surface of the sample ($z = 0$) is

$$T_{\mathrm{HAM}}(r,0,t) = T_0 \int_0^\infty f_{\mathrm{HAM}}(a,t) J_0(r\alpha) J_1(\omega_{0e}\alpha)\, d\alpha \qquad (6)$$

with

$$f_{\mathrm{HAM}}(\alpha,t) = 2\sqrt{t_c/\pi} \int_0^t \tau^{-1/2} \exp\left(\frac{-\alpha^2\omega_{0e}^2\tau}{4t_c} \right) d\tau = \frac{4t_c}{\alpha\omega_{0e}}\,\mathrm{Erfc}\left(\frac{\alpha\omega_{0e}}{2\sqrt{t_c/\tau}} \right). \qquad (7)$$

In order to analyze the applicability of the extreme cases, Fig. 4 shows the numerical comparison between LAM and BLM as well as between HAM and BLM in terms of the normalized temperature rise changing with the absorption coefficient. We can see that for $A_e < 200\ \mathrm{m}^{-1}$ the agreement between the LAM and the BLM is very good with the difference less than 5%. On the other hand, for $A_e > 10^5\ \mathrm{m}^{-1}$ the difference between HAM and the BLM is less than 6%. For $200 < A_e < 10^5\ \mathrm{m}^{-1}$ the BLM should be used.

2.2 Surface displacement/deformation

The laser induced temperature rise causes the displacement on sample surface (thermoelastic deformation). In the quasi-

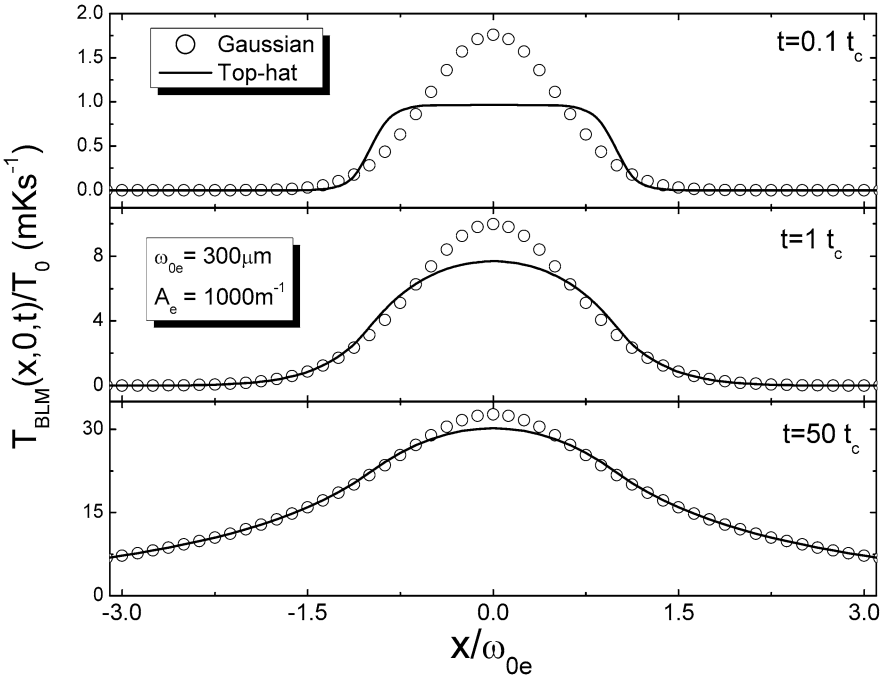

Fig. 3 Normalized radial temperature rise profiles with $y = 0$ using top-hat and Gaussian beam excitation for $t = 0.1t_c$, $t = 1t_c$, and $t = 50t_c$

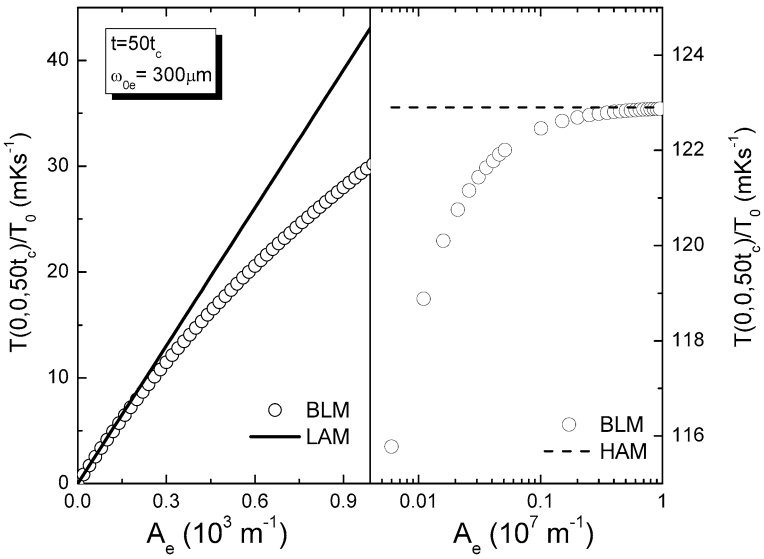

Fig. 4 Normalized temperature rise at the sample surface for $x = y = z = 0$ as a function of the absorption coefficient A_e. The parameters used for the simulations are indicated in the figure. LAM was numerically calculated using (1) of [19], and BLM and HAM by using (4) and (6), respectively

static approximation, the thermoelastic equation for the surface deformation caused by a laser-induced non-uniform temperature distribution is given by [21]

$$(1-2\nu)\nabla^2\mathbf{u} + \nabla(\nabla.\mathbf{u}) = 2(1+\nu)\alpha_T \nabla T(r,z,t). \tag{8}$$

The boundary conditions at the free surface are $\sigma_{rz}|_{z=0} = 0$ and $\sigma_{zz}|_{z=0} = 0$ [21]. Here $\mathbf{u}$ is the displacement vector, α_T the linear thermal expansion coefficient, ν the Poisson's ratio, and σ_{rz} and σ_{zz} are the normal stress components.

The solution of (8) can be expressed by introducing the scalar displacement potential Ψ and the Love function ψ as [21]

$$\mathbf{u}(r,t) = \nabla\Psi(r,t) - \nabla\times\left[\frac{\partial\psi(r,t)}{\partial r}e_\theta\right]. \tag{9}$$

Ψ and ψ are governed by the Poisson equation

$$\nabla^2\Psi(r,z,t) = \chi T(r,z,t), \tag{10}$$

with $\chi = \alpha_T(1+\nu)/(1-\nu)$, and by the biharmonic equation

$$\nabla^2\nabla^2\psi(r,z,t) = 0. \tag{11}$$

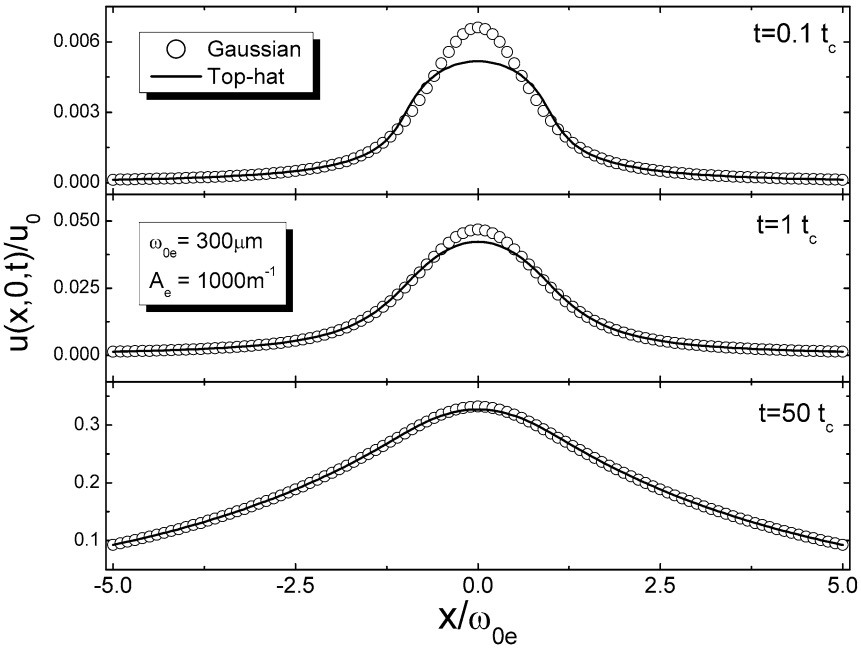

Fig. 5 Radial profiles of normalized surface deformation with $y = z = 0$ using top-hat and Gaussian beam excitation lasers for $t = 0.1t_c$, $t = 1t_c$, and $t = 50t_c$ ($A_e = 1000\ \mathrm{m}^{-1}$ and $\omega_{0e} = 300\ \mu\mathrm{m}$)

From the solution of (10) and (11), and the evaluation of the stress components [21], the displacement can be calculated by using the given temperature distribution.

Using (4) and (5) for the BLM and (6) and (7) for the HAM, the z-component of u at the sample surface ($z = 0$) takes the form

$$u_z(r,0,t) = \frac{-u_0}{4\omega_{0e}t_c}\int_0^\infty h(\alpha,t)J_0(r\alpha)J_1(\omega_{0e}\alpha)\,d\alpha. \qquad (12)$$

For the BLM, $h(\alpha,t)$ is

$$\begin{aligned} h_{\mathrm{BLM}}(\alpha,t) &= \frac{tA_e^2\omega_{0e}^2}{A_e^2-\alpha^2}\,\mathrm{Erfc}\left(\frac{\alpha\omega_{0e}}{2\sqrt{t_c/t}}\right) \\ &+ \frac{2\sqrt{t_c t/\pi}\,\omega_{0e}A_e^2}{(\alpha^3-\alpha A_e^2)}\exp\left(-\frac{t\alpha^2\omega_{0e}^2}{4t_c}\right) \\ &+ \frac{2A_e t_c}{\alpha^2(\alpha^2-A_e^2)^2}\left\{\left(A_e^3-3\alpha^2A_e\right)\mathrm{Erf}\left(\frac{\alpha\omega_{0e}}{2\sqrt{t_c/t}}\right)\right. \\ &\left. + 2\alpha^3\left[1-\exp\left(\frac{(A_e^2-\alpha^2)\omega_{0e}^2}{4t_c/t}\right)\mathrm{Erfc}\left(\frac{A_e\omega_{0e}}{2\sqrt{t_c/t}}\right)\right]\right\}, \end{aligned} \qquad (13)$$

and for the HAM it is

$$\begin{aligned} h_{\mathrm{HAM}}(\alpha,t) &= t\omega_{0e}^2\,\mathrm{Erfc}\left(\frac{\alpha\omega_{0e}}{2\sqrt{t_c/t}}\right) - \frac{2\sqrt{t_c t}\,\omega_{0e}}{\sqrt{\pi}\alpha}\exp\left(\frac{-\alpha^2\omega_{0e}^2}{4t_c/t}\right) \\ &+ \frac{2t_c}{\alpha^2}\,\mathrm{Erf}\left(\frac{\alpha\omega_{0e}}{2\sqrt{t_c/t}}\right), \end{aligned} \qquad (14)$$

in which $u_0 = 2P_e\alpha_T(1+\nu)\phi/(\pi k)$, and $\mathrm{Erf}(x)$ and $\mathrm{Erfc}(x)$ are the error function and complementary error function, respectively. The displacement vector **u** at the sample surface ($z = 0$) for the LAM can be found in [19], (4) and (5).

In the same way as previously discussed about the temperature rise profiles, we compare the normalized deformation on the sample surface ($z = 0$) induced by a top-hat excitation laser with that produced by a Gaussian laser, as shown in Fig. 5. We use (12) and (13) for the top-hat beam excitation and (2) and (3) of [13] for the Gaussian one for the numerical simulation of the BLM. Similar to the temperature rise profiles, for a time less than t_c, the deformation profiles follow the excitation laser profiles. The maximum deformation caused by the Gaussian laser excitation, at the center of the beam, is higher than that caused by the top-hat one. For $t = 50t_c$, the deformation profiles for both top-hat and Gaussian excitations are approximately the same.

Figure 6 shows the maximum deformations caused by the top-hat and Gaussian excitations, at the center of the beam, as a function of the excitation laser radius. With $\omega_{0e} = 300\ \mu\mathrm{m}$ the maximum deformation caused by the top-hat laser excitation is about 2% less than that produced by the Gaussian one. The difference decreases rapidly with the decrease of the excitation laser radius. The numerical calculations of the temperature rise (Fig. 3) and surface deformation (Fig. 5) indicate that the top-hat thermal mirror technique has the sensitivity comparable to that of the Gaussian one.

Concerning the extreme cases, the main advantage of using the LAM and HAM is the simplification of the equation solutions and the numerical calculations over u_z. Figure 7 shows the calculated surface deformation using the

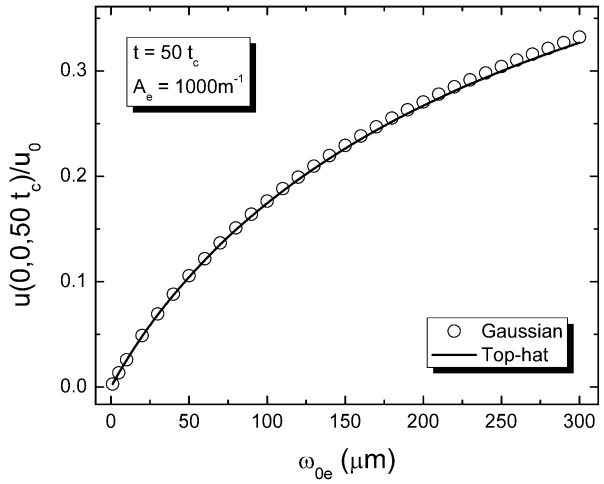

Fig. 6 Calculated surface deformations at $x = y = z = 0$ using top-hat and Gaussian laser excitation for $t = 50t_c$ and $A_e = 1000\ \mathrm{m}^{-1}$

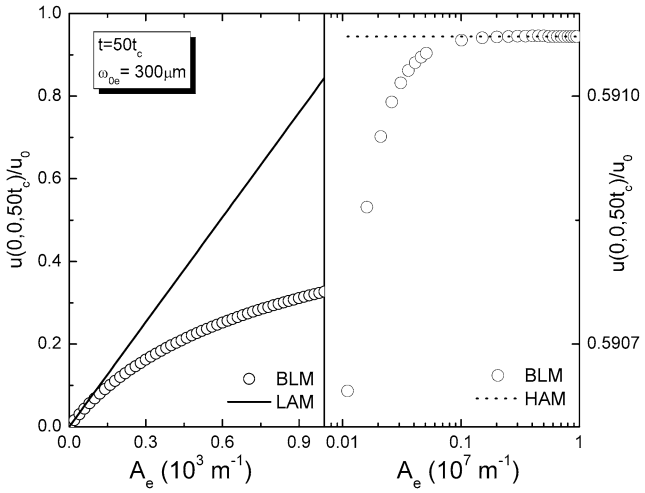

Fig. 7 Surface deformation for $x = y = z = 0$ as a function of the optical absorption coefficient ($t = 50t_c$). The LAM was numerically calculated using (2) and (3) of [19], and the BLM and HAM was computed by using (12) and (13) as well as (12) and (14), respectively

complete the BLM compared with the LAM and HAM as a function of the optical absorption coefficient up to $10^7\ \mathrm{m}^{-1}$. For $A_e < 150\ \mathrm{m}^{-1}$, the agreement between the LAM and the BLM is very good with the relative difference less than 10%. For $A_e > 10^5\ \mathrm{m}^{-1}$, the HAM can be used to describe the surface deformation, and the largest difference is less than 1%.

2.3 Probe beam phase shift and TM signal

The deformation produced on the sample surface acts as an optical element, causing a phase shift to the electric field of the reflected probe beam. The phase shift is given by [12–19]

$$\Phi = \frac{2\pi}{\lambda_P} 2u_z(r, 0, t). \tag{15}$$

With the phase shift, the TEM_{00} Gaussian probe beam reflected by the surface displacement/deformation propagates to the plane of a detector. Using Fresnel diffraction theory, one can find the center point of its complex electric field at the far field detector plane [12–19, 22]

$$U(Z_1 + Z_2, t) = B \int_0^\infty \exp\left[-(1 + iV)g - i\Phi(g, t)\right] dg, \tag{16}$$

in which B is a constant [19], $g = (r/\omega_{1P})^2$ and $V = Z_1/Z_C$ [23]. For the BLM and HAM $\Phi(g, t)$ can be expressed as

$$\Phi_{\mathrm{BLM}}(g, t) = \frac{\theta_{\mathrm{TM}}}{\omega_{0e} t_c} \int_0^\infty h_{\mathrm{BLM}}(\alpha, t) J_0(\omega_{0e}\alpha\sqrt{mg}) J_1(\omega_{0e}\alpha)\, d\alpha, \tag{17}$$

$$\Phi_{\mathrm{HAM}}(g, t) = \frac{\theta_{\mathrm{TM}}}{\omega_{0e} t_c} \int_0^\infty h_{\mathrm{HAM}}(\alpha, t) J_0(\omega_{0e}\alpha\sqrt{mg}) J_1(\omega_{0e}\alpha)\, d\alpha, \tag{18}$$

in which

$$\theta_{\mathrm{TM}} = -\frac{2P_e\alpha_T(1 + \nu)}{\lambda_P k}\phi. \tag{19}$$

Here, $m = \omega_{1P}^2/\omega_{0e}^2$. The parameter m provides the degree of the mismatching between the probe and the excitation beams.

Substituting (17), (13) and (18), (14) for the $\Phi_{\mathrm{BLM}}(g, t)$ and $\Phi_{\mathrm{HAM}}(g, t)$, respectively, into (16) and carrying out numerical integration over g, the intensity $I(t)$ can be calculated as $I(t) = |U(Z_1 + Z_2, t)|^2$ [12–19, 22]. The solution for the LAM can be found in [19]. The temporal evolution of the TM signal depends on the characteristic TM thermal time constant, t_c, which is related to the thermal diffusivity, and on the amplitude of the TM signal, θ_{TM}, which is correlated to the thermo-mechanical properties of the sample.

3 Experimental results and discussions

Figure 8 shows a schematic diagram of the experimental apparatus used for the TM experiment. A multi-mode diode-pumped solid-state laser (Melles Griot, Model 85 GLS 309, 532.0 nm) was employed to provide the top-hat beam excitation. The excitation beam was expanded by a set of lens. A pupil was employed to select a nearly homogeneous area of the expanded excitation beam, and the homogenized excitation beam passed through a lens to produces a top-hat intensity profile on the sample. The radius of the excitation laser beam at the sample position was determined

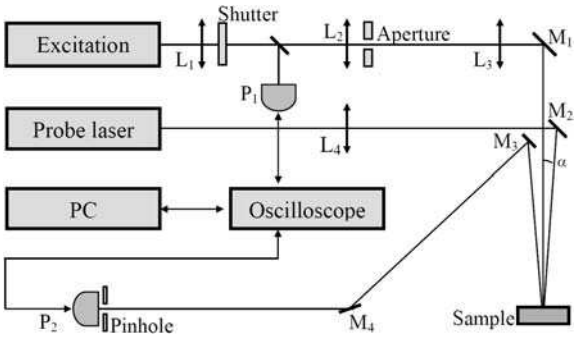

Fig. 8 A schematic diagram of an apparatus for time-resolved TM experiments. The excitation and probe beams were provided by a diode pumped solid-state laser (532 nm) and a He–Ne laser (632.8 nm), respectively. M_i, L_i, and P_i stand for mirrors, lenses and photodiodes, respectively

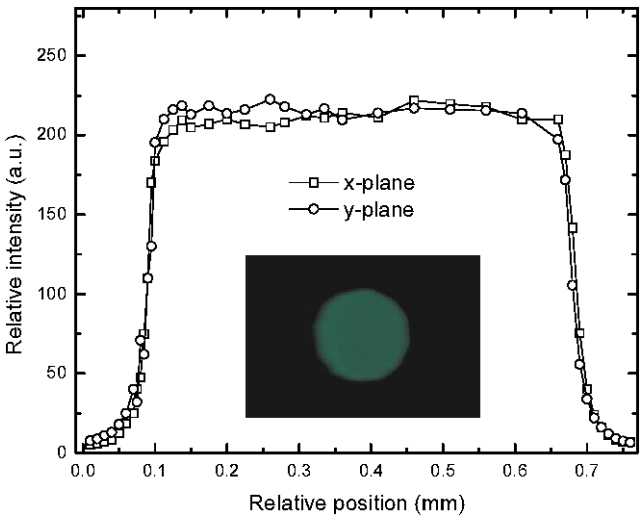

Fig. 9 The cross-section profiles of the top-hat excitation laser beam on x–y plane. The *inset* shows the typical top-hat profile of the excitation laser beam at the sample surface

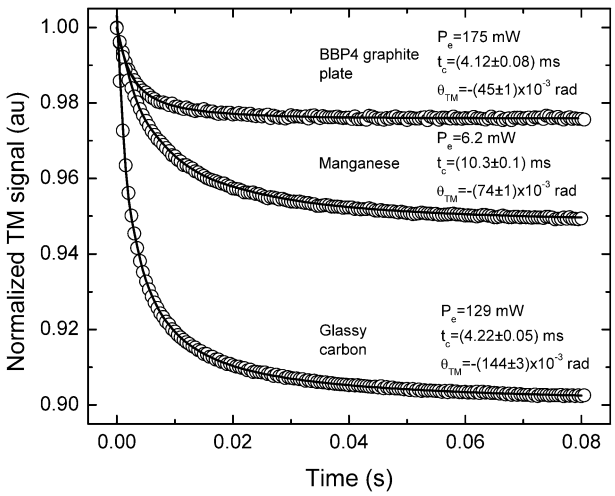

Fig. 10 Normalized TM signals $I(t)/I(0)$ for the samples. *Open dots*: experimental data; *solid lines*: best curve fitting using the HAM

by measuring its transverse intensity distribution using a pinhole-photodiode assembly. The diameter of the pinhole was 5 µm. Exposure of the sample to the excitation beam was controlled by a shutter (ThorLabs, Model SH05), and the signal from the photodiode P_1 was used to trigger a digital oscilloscope (Tektronics, Model TDS 3052) to record the TM signal. A weak TEM_{00} Gaussian He–Ne laser at 632.8 nm (Melles Griot, Model 05LHP151) or 543.5 nm (Melles Griot, Model 05LGP193), almost collinear to the excitation beam ($\alpha < 1.5°$), probed the TM by examining the intensity of the reflected probe beam. The probe beam was focused by lens L_4 ($f = 20$ cm), and the sample was positioned near its confocal plane. After reflected by the TM, the probe beam propagated to a photodiode P_2 positioned in a far field ($Z_2 \approx 5$ m). A pinhole was put in front of the photodiodes P_2, and only the central part of the probe beam was detected by the photodiode and then recorded by a digital oscilloscope. The parameters ω_{1P}, Z_C and Z_1 were measured as described in [22].

To show the applicability of the complete BLM and the HAM, we performed measurements of opaque samples: manganese metal (99.9% from Sigma-Aldrich), glassy carbon, and BBP4 graphite plate. BBP4 graphite plate is an anisotropic sample used for fabricating bipolar plates of proton exchange membrane fuel cells. The samples were cut approximately 1 cm in diameter and their surfaces were fine polished to create a high reflective surface. The optical reflection coefficients of the three samples were determined by measuring the incident and reflected power at the excitation wavelength and used to correct the absorbed power P_e by the samples.

In this work, the geometrical parameters for the probe beam used in the experiments for the glassy carbon and for the manganese metal were $\lambda_p = 543.5$ nm, $\omega_{1P} = 1015$ µm, $Z_1 = 297$ mm, $Z_C = 15$ mm, $V = 20.0$, $\omega_{0e} = 295$ µm, and $m = 11.8$. For BBP4 graphite plate, $\lambda_p = 632.8$ nm, $\omega_{1P} = 1285$ µm, $Z_1 = 387$ mm, $Z_C = 15$ mm, $V = 25.8$, $\omega_{0e} = 387$ µm, and $m = 11$ were used. Figure 9 shows the cross-section profiles of the top-hat excitation beam on x–y plane. The beam diameters along the two directions are approximately the same, (0.59 ± 0.01) mm. The inset of Fig. 9 shows the intensity profile of the excitation laser beam at the sample surface recorded with a CCD camera.

Figure 10 shows normalized transients of the TM signals of the samples. The used excitation powers to generate the TM effects are listed in the figure. For all three samples, the probe beam reflected from the TM is defocused, which means the thermal expansion coefficients are positive. The numerical curve fitting of the TM transients to the HAM, corresponding to the solid lines in Fig. 10, deduced the values of t_c that is related to the thermal diffusivity and θ_{TM} which is associated with thermo-mechanical properties. Us-

Table 1 The results of the TM experimental measurements

Samples	D (Measured) (10^{-8} m^2 s^{-1})	D (Literature) (10^{-8} m^2 s^{-1})	E (Measured) (10^3 W s$^{1/2}$ m^{-2} K^{-1})	$k = E\sqrt{D}$ (Measured) (W mK)$^{-1}$	$k = E\sqrt{D}$ (Literature) (W mK)$^{-1}$
Glassy carbon	5.20 ± 0.03	5.0 [26]	3.60 ± 0.02 [25]	8.20 ± 0.09	8 [26]
BBP4 graphite plate	8.93 ± 0.08	8.8*	7.0 ± 0.3 [25]	20.9 ± 0.2	21*
Manganese	2.07 ± 0.04	2.3 [24]	5.3 [24]	7.60 ± 0.07	8 [24]

*Typical values from the vendor

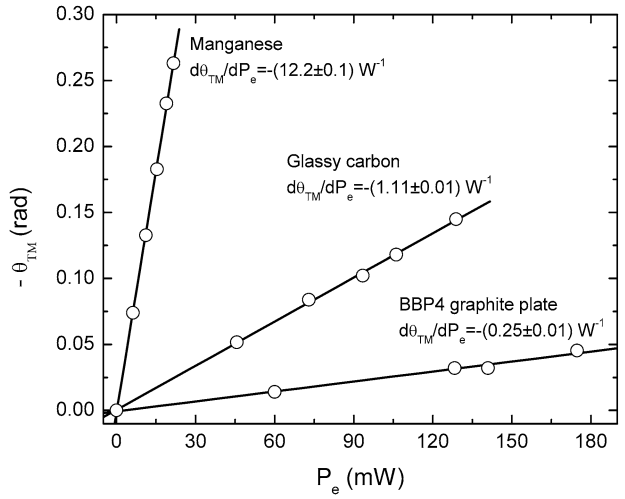

Fig. 11 The fitted θ_{TM} as a function of excitation power for TM experiments

Table 2 The results of the TM experimental measurements

Samples	$d\theta_{\mathrm{TM}}/dP_e$ (Measured) (W^{-1})	ν (Literature)	α_T (Measured) (10^{-6} K^{-1})
Glassy carbon	$-(1.11 \pm 0.01)$	0.20*	2.0 ± 0.1
BBP4 graphite plate	$-(0.25 \pm 0.01)$	0.20*	1.40 ± 0.05
Manganese	$-(12.2 \pm 0.1)$	0.23 [24]	21.1 ± 0.6

*Typical values from vendors

ing $t_c = \omega_{0e}^2/4D$, the thermal diffusivities of the samples were calculated as shown in Table 1, consistent with the literature values [24, 25].

The measurements were performed with different excitation powers, and the linear dependences of the θ_{TM} on the power were also obtained by the curve fitting, as shown in Fig. 11. Table 2 shows the values of the slopes $d\theta_{\mathrm{TM}}/dP_e$ of the samples.

Additional measurements were performed using the photothermal deflection method (PDS) as described in [25] to determine the thermal effusivities of these samples. With the thermal effusivity and using the relation $k = E\sqrt{D}$ [25], we calculate the thermal conductivity of the samples (Table 1). Referring to (19) for the θ_{TM} and using the measured $d\theta_{\mathrm{TM}}/dP_e$, k and the literature value of ν, the expansion coefficient can be determined as $\alpha_T = -(d\theta_{\mathrm{TM}}/dP_e)\lambda_P k/[\phi(1+\nu)]$. For the samples studied in this work, $\phi = 1$, meaning all the absorbed energy by the samples is converted into heat. The results of the $\alpha_T s$ are shown in Table 2. For the manganese sample it is in good agreement with the literature value [24]. For the glassy carbon and BBP4 graphite plate, the determined values are similar to those ones of this class of the materials ([26] and [25], respectively).

4 Conclusions

We presented a completed theoretical model for top-hat laser induced time-resolved TM technique. The thermoelastic deformation on the sample surface and the center intensity of the probe beam at the detector plane were derived. To simplify the theory, the LAM and HAM were compared with the completed theory to find their suitable application ranges of optical absorption of a sample. An experimental apparatus was set up to determine the thermo-physical properties of the samples, and the experimental results were found to be consistent with the literature values, validating the theoretical model. Furthermore, numerical simulations indicate that the top-hat laser induced TM is as sensitive as that produced by Gaussian beam excitation. The theoretical model and experimental apparatus developed in this work make it promising to use a top-hat laser in TM and other photothermal experiments and to expand the applicability of photothermal science and techniques with a less expensive non-Gaussian excitation laser.

References

1. A. Mandelis (ed.), *Progress in Photoacoustic and Photothermal Science and Technology* (Elsevier, New York, 1991)
2. D.P. Almond, P.M. Patel, *Photothermal Science and Techniques* (Chapman & Hall, London, 1996)

3. S.E. Bialkowski, *Photothermal Spectroscopy Methods for Chemical Analysis* (Wiley, New York, 1996)
4. M.A. Olmstead, N.M. Amer, S. Kohn, D. Fournier, A.C. Boccara, Appl. Phys. A **32**, 141 (1983)
5. J. Opsal, A. Rosencwaig, D.L. Willenborg, Appl. Opt. **22**, 3169 (1983)
6. B.C. Li, J. Appl. Phys. **68**, 482 (1990)
7. B.C. Li, S. Xiong, Y. Zhang, Appl. Phys. B **80**, 527 (2005)
8. J.W. Fang, S.Y. Zhang, Appl. Phys. B **67**, 633 (1998)
9. P. Kuo, M. Munidasa, Appl. Opt. **29**, 5326 (1990)
10. H. Saito, M. Irikura, M. Haraguchi, M. Fukui, Appl. Opt. **31**, 2047 (1992)
11. J.W. Fang, S.Y. Zhang, Appl. Phys. B **67**, 633 (1998)
12. N.G.C. Astrath, L.C. Malacarne, P.R.B. Pedreira, A.C. Bento, M.L. Baesso, J. Shen, Appl. Phys. Lett. **91**, 191908 (2007)
13. L.C. Malacarne, F. Sato, P.R.B. Pedreira, A.C. Bento, R.S. Mendes, M.L. Baesso, N.G.C. Astrath, J. Shen, Appl. Phys. Lett. **92**, 131903 (2008)
14. F. Sato, L.C. Malacarne, P.R.B. Pedreira, M.P. Belancon, R.S. Mendes, M.L. Baesso, N.G.C. Astrath, J. Shen, J. Appl. Phys. **104**, 053520 (2008)
15. B. Li, S. Martin, E. Welsch, Opt. Lett. **24**, 1398 (1999)
16. B. Li, S. Martin, E. Welsch, Appl. Opt. **39**, 4690 (2000)
17. B. Li, X. Chen, Y. Gong, J. Appl. Phys. **103**, 033518 (2008)
18. N.G.C. Astrath, F.B.G. Astrath, J. Shen, J. Zhou, P.R.B. Pedreira, L.C. Malacarne, A.C. Bento, M.L. Baesso, Opt. Lett. **33**, 1464 (2008)
19. F.B.G. Astrath, N.G.C. Astrath, J. Shen, J. Zhou, L.C. Malacarne, P.R.B. Pedreira, M.L. Baesso, Opt. Express **16**, 12214 (2008)
20. H.S. Carslaw, J.C. Jaeger, *Conduction of Heat in Solids*, vol. 1 (Clarendon, Oxford, 1959), p. 78
21. W. Nowacki, *Thermoelasticity*, vol. 3 (Pergamon, Oxford, 1982), p. 11
22. M.L. Baesso, A.C. Bento, A.A. Andrade, J.A. Sampaio, E. Pecoraro, L.A.O. Nunes, T. Catunda, S. Gama, Phys. Rev. B **57**, 10545 (1998)
23. J. Shen, R.D. Lowe, R.D. Snook, Chem. Phys. **165**, 385 (1992)
24. D.R. Lide, *CRC Handbook of Chemistry and Physics*, 88th edn. (CRC Press, Cleveland, 1977)
25. F.B.G. Astrath, N.G.C. Astrath, J. Shen, J. Zhou, M.L. Baesso, J. Appl. Phys. **104**, 066101 (2008)
26. J. Shen, J. Zhou, C. Hu, J. Zhao, Appl. Spectrosc. **57**, 186 (2003)